Ore Geology Reviews 118 (2020) 103354

Contents lists available at ScienceDirect

Ore Geology Reviews

journal homepage: www.elsevier.com/locate/oregeorev

Fluid inclusion and stable isotope (C, O and S) constraints on the genesis of the high-grade Langdu Cu skarn deposit in Yunnan, SW China

Tao Ren[a,b], Hong Zhong[a,*], Xing-chun Zhang[a]

[a] State Key Laboratory of Ore Deposit Geochemistry, Institute of Geochemistry, Chinese Academy of Sciences, Guiyang 550018, China
[b] Faculty of Land Resources Engineering, Kunming University of Science and Technology, Kunming 650093, China

ARTICLE INFO

Keywords:
High-grade Cu skarn deposit
C–O–S isotopes
Fluid inclusions
Zhongdian area
SW China

ABSTRACT

The Langdu Cu skarn deposit is the highest grade Cu deposit (average 6.49% Cu) in the Zhongdian polymetallic district in SW China. Skarns and ore bodies occur primarily in the contact zone of Upper Triassic Qugasi Formation (Fm.) and Late Triassic (ca. 217 Ma) intrusions. Disseminated, massive, stockwork, and vein-like sulfide ores occur in the skarn, quartz-calcite veins, porphyry and marble. Skarn minerals include pyroxene, garnet, actinolite, and epidote. Four types (six subtypes) of fluid inclusions (FIs) are identified in the sulfide-bearing quartz veins. Type-I liquid-rich two phase FIs have varying vapor/liquid ratios, and yielded homogenization temperatures of 110–338 °C and salinities of 1.7–29.5 wt% NaCl eqv. Type-II vapor-rich FIs contain CH_4-N_2 bubbles and homogenized to vapor at 262–425 °C. Type-III FIs are single phase at room temperature (20 °C). A vapor phase is present at below −120 °C, and the FIs homogenized at −117 to −114 °C. Type-IV daughter mineral-bearing FIs homogenized by halite disappearance at 295–392 °C, and have salinities of 37.8–46.6 wt% NaCl eqv. Such characteristics suggest that FIs were trapped by fluid immiscibility and phase separation. The $\delta^{34}S_{CDT}$ values of chalcopyrite and pyrrhotite are of −5.3 to 0.7‰. On the $\delta^{34}S$ histogram, all Langdu data show a cluster of ^{32}S-rich ($\delta^{34}S_{CDT}$ = −5.3 to −4.6‰) and a cluster of ^{34}S-rich ($\delta^{34}S_{CDT}$ = −1.1 to 0.7‰). Type-I calcite (in skarn) and type-II calcite (in quartz-sulfide vein) have $\delta^{13}C_{PDB}$ and $\delta^{18}O_{SMOW}$ values of −8.4 to −7.8‰, −6.3 to −6.1‰ and 10.1 to 12.3‰ and 12.0 to 13.0‰, respectively. Type-III calcite from calcite-sulfide veins has $\delta^{13}C_{PDB}$ = −5.6 to 0.2‰ and $\delta^{18}O_{SMOW}$ = 12.5 to 16.3‰. Biotite, garnet and pyroxene, syn-ore quartz, and chlorite yielded $\delta^{18}O_{SMOW}$ values of 6.9‰, 4.1–5‰, 13.2–15.3‰, and 6.8‰, respectively. Sulfur, carbon and oxygen isotopic features of these hydrothermal minerals and the FIs microthermometric data suggest that the ore-forming fluids were magmatic sourced and contaminated by meteoric/formation water during ascent and/or fluid/wallrock interactions. Low $\delta^{34}S$ (= −5.3 to −4.6‰) in sulfides and the CH_4 in the FIs are interpreted to reflect the reaction between the magmatic fluids and the carbonaceous slate in Qugasi Fm. The methane likely expanded the vapor/liquid immiscibility field and reduced the sulfates (SO_4^{2-}) to sulfides (S^{2-}). And extensive water/rock reaction and fluid mixing may have occurred, leading to the high-grade Cu mineralization at Langdu.

1. Introduction

The Zhongdian area located in the southern Yidun island arc is a key porphyry-related Cu polymetallic province in China (Fig. 1a–b). Many deposits in the region were interpreted to be Late Triassic intrusion-related (Wang et al., 2007; Leng et al., 2012, 2014; Wang et al., 2014). Major deposits include the Pulang, Xuejiping, Lannitang and Chundu porphyry Cu (–Au) deposits, and the Langdu and Gaochiping Cu skarn deposits. In addition, the Relin and Xiuwacu W–Mo deposits, and the Hongshan and Tongchanggou Cu (–Mo) deposits were considered to be related to the Late Cretaceous monzonites and porphyritic granites (Fig. 1c; Wang et al., 2007; Wang et al., 2014). Among these Cu deposits, the Pulang is the largest and contains metal reserves of 436 Mt Cu (Wang et al., 2007).

The Langdu Cu skarn deposit is located in the northeastern Zhongdian polymetallic district (Fig. 1c). Alteration zonation can be clearly seen from the ore-causative porphyry to the limestone wallrocks at Langdu. Deposit geology and mineralogy of the Langdu deposit were described by many authors (e.g., Yang et al., 2002; Hou et al., 2004; Zeng et al., 2004), yet the mineral assemblages, ore textures, skarn mineral chemistry and the source and evolution of ore-forming fluids are still unclear. In particular, the source of CH_4 in the ore-forming

* Corresponding author.
E-mail address: zhonghong@vip.gyig.ac.cn (H. Zhong).

https://doi.org/10.1016/j.oregeorev.2020.103354
Received 4 November 2019; Received in revised form 30 December 2019; Accepted 19 January 2020
Available online 23 January 2020
0169-1368/

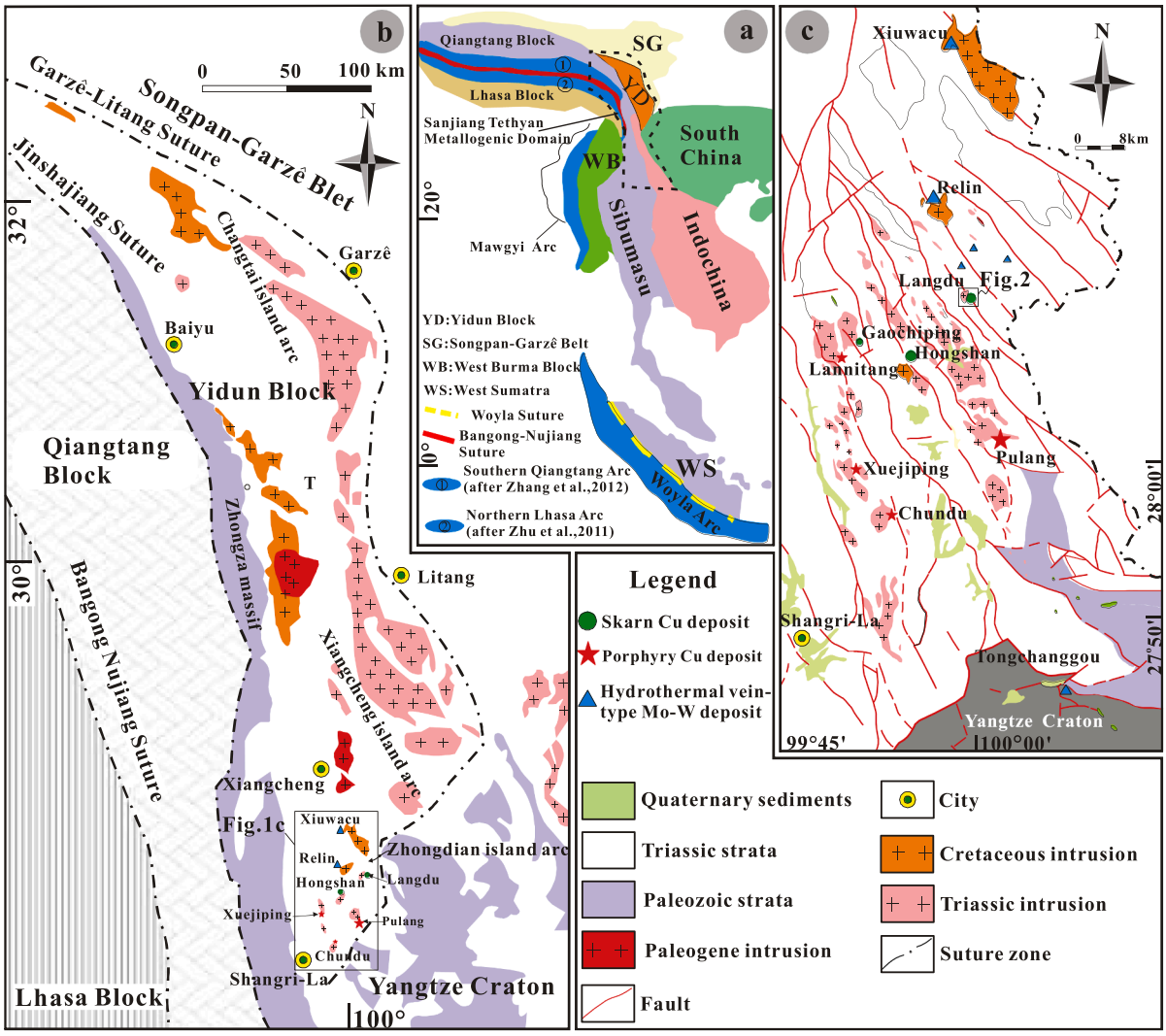

Fig. 1. (a) Regional location map showing tectonic blocks accreted in the Late Paleozoic (Hou et al., 2007; Morley, 2012; Zhang et al., 2012; Zhu et al., 2011), simplified geologic maps of (b) the Yidun block (modified after Hou et al., 2007) and (c) Zhongdian area, showing the locations of the Langdu and other deposits.

fluids and its metallogenic role remain poorly understood, as well as the cause of the high Cu grade (average 6.49% Cu).

In this study, new major element data of the skarn minerals, microthermometric data of the quartz-hosted FIs, and data of carbon-oxygen (C–O) isotopes of hydrothermal calcite, sulfur (S) isotopes of sulfides, and oxygen isotopes of biotite, garnet, pyroxene, quartz, and chlorite were presented to discuss the ore genesis and cause of high-grade Cu mineralization at Langdu.

2. Regional geology

The Tibetan plateau comprises a number of microcontinental blocks and island arcs, including the E-W-trending Songpan-Garzê belt and the Yidun, Qiangtang and Lhasa blocks. The Yidun block is bound by the Garzê-Litang suture to the east and the Jinshajiang suture to the west. The Jinshajiang suture may have formed during the Early-Middle Triassic, and the Garzê-Litang suture during the Late Triassic (Hou et al., 2004; Leng et al., 2012, 2014; Wang et al., 2014; Guo et al., 2020).

The Yidun block comprises the Zhongza massif and Yidun island arc (Fig. 1b). Geochemical and geochronological evidences suggest that the Zhongza massif was separated from the Yangtze craton in the Late Permian (Leng et al., 2012, 2014, 2018; Wang et al., 2014; Tian et al., 2019). The Yidun island arc was formed by the subduction of the Garzê-Litang ocean basin and covered by upper Triassic flysch and mafic-felsic volcanic arc-like rocks. From north to south, the Yidun island arc comprises the Changtai, Xiangcheng, and Zhongdian arcs (Fig. 1b).

Calc-alkaline volcanic and intrusive rocks were emplaced during the subduction of Garzê-Litang oceanic basin (Leng et al., 2012). Volcanic rocks in the Zhongdian arc include andesite in the Upper Triassic Tumugou Formation (Fm.), and basalt and basaltic andesite in the Upper Triassic Qugasi Fm. Late Triassic diorite, monzonite, dacite, and granodiorite porphyry occur in the northwestern part of Zhongdian arc. Late Cretaceous granites are distributed in the northern and southern parts of the region (Fig. 1c; Leng et al., 2012, 2014; Wang et al., 2014).

3. Ore deposit geology

The Langdu Cu skarn deposit was discovered in 1964 by the Yunnan Bureau of Geology and Mineral Resources (BGMR). Several Cu-rich orebodies are recently delineated along the intrusive contact between the monzonite porphyries and marble to the north and west of the original Langdu mine. The deposit contains 0.1 Mt Cu, with an average Cu grade of 6.49 wt%.

3.1. Strata and intrusions

Exposed stratigraphy at Langdu mainly comprises the Upper Triassic

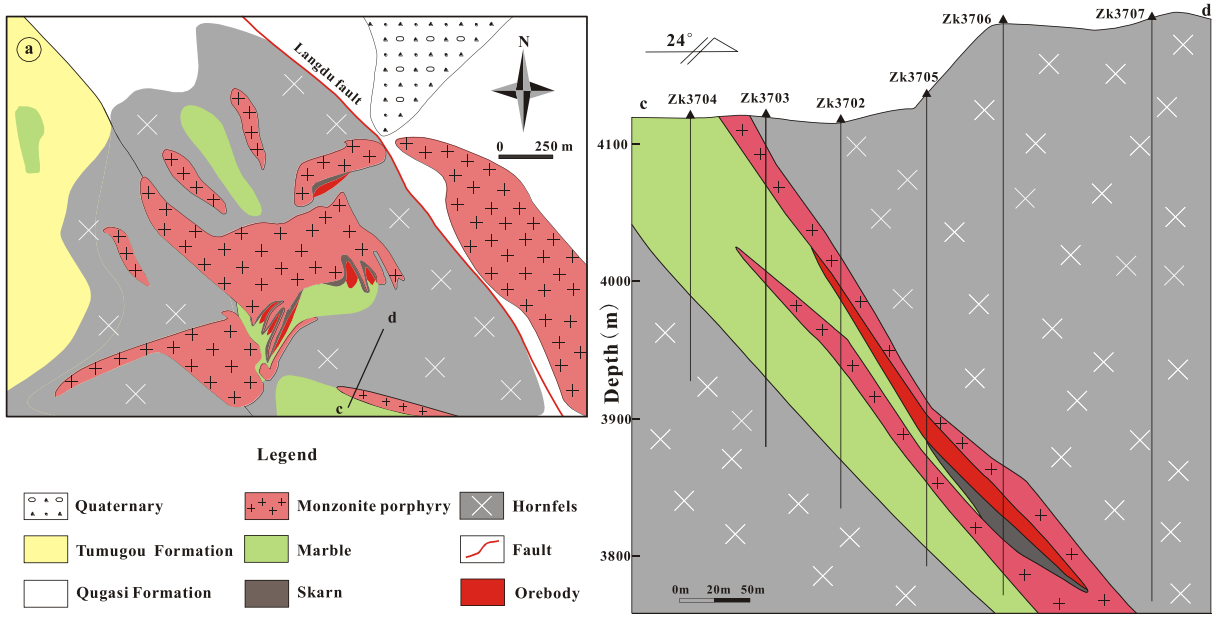

Fig. 2. (a) Geologic map of the Langdu deposit, showing the locations of porphyries, alteration zones, orebodies and faults (Ren et al., 2010) and (b) geologic section along Exploration Line 37 at Langdu deposit.

Qugasi and Tumugou Formations (Fig. 2a). The Qugasi Formation (total thickness = 487–2683 m) contains limestone, carbonaceous slate, and sandstone (Fig. 2a; Ren et al., 2013). The conformably-overlying Tumugou Formation is exposed in the southwestern Langdu (Fig. 2a), with a thickness of 1433 m. Tumugou Formation is mainly composed of slate and sandstone with minor limestone occurring as thin layers or lenses (Ren et al., 2013).

Monzonite porphyries are widely exposed in the mining area (Fig. 2a). Previous studies show that these rocks are high-K calc-alkaline and emplaced at 217 ± 4 Ma (Zeng et al., 2004). The rocks may have formed by partial melting of the slightly enriched mantle, triggered by the subdution of the Garzê-Litang Ocean, and contaminated by slab-derived fluids or sediments (Ren et al., 2010, 2013). Potassic alteration is locally observed in the intrusions (Fig. 4a), forming an assemblage of secondary K-feldspar + biotite + quartz. The secondary K-feldspar with fine-grained biotite rims around the original K-feldspar phenocryst, or locally occurs as K-feldspar + quartz veinlet (Fig. 4b).

3.2. Skarn and mineralization

The emplacement of porphyritic intrusive resulted in contact metamorphism of the clastic rock and limestone to hornfel and marble, respectively, and locally metasomatized the carbonate rock to skarn (Fig. 2a). The hydrothermal-metasomatic sequences include prograde and retrograde skarns (Fig. 3). Hydrothermal alteration occurs in narrow halos around the intrusive contact of the Qugasi Formation (Fig. 2b, 4a). Alteration mineral (or metamorphic rock) zoning (from intrusion to limestone) comprises: pyroxene + actinolite + epidote + sulfide → garnet + actinolite + sulfide → quartz + calcite + sulfide → marble (Figs. 3 and 4a).

In pyroxene + actinolite + epidote + sulfide zone, pyroxene is coarse-grained (Fig. 4c) and locally replaced by fibrous actinolite (Figs. 5a–b, 6a), and has a composition of $Hd_{78-92}Di_{3-11}Jo_{5-11}$ (Table 1; Fig. 6a). Concentrations of certain trace elements in the pyroxene (e.g., Ti and Cr) are only slightly above their detection limits. In contrast, the Mn contents are high, and Fe/Mn ratios vary between 7.15 and 19.80 (average 15.44). Retrograde epidote occurs as radial aggregate (Fig. 4d). Quartz-sulfide (chalcopyrite, pyrrhotite) veins/in-fills are found in the vugs and fractures of pyroxene (Fig. 4g).

In the garnet + actinolite + sulfide zone (Fig. 4A), coarse-grained reddish-brown idiomorphic (Fig. 4e) and fine-grained xenomorphic garnets (Fig. 4f) are observed. The garnets show optical and compositional zoning (Fig. 5d, e), and have varying compositions ($Ad_{57-94}Gr_{5-41}Spe_{0.4-1}$; Table 2; Fig. 6b), with their Al and Fe contents in increase and decrease from core to rim, respectively. Irregularly shaped type-I calcite infills are found in mineral fractures (Fig. 4f). Vein/fibrous actinolite (partially) replaced and crosscut the euhedral garnet (Fig. 4e, 5c). Although grunerite and actinolite are difficult to distinguish under the optical microscope, they can be easily identified in BSE (backscattered electron) image, as grunerite appears darker than actinolite (Fig. 5f).

Copper orebodies at Langdu occur primarily as veins or lenses in the contact zone between the monzonite porphyries and limestone/marble (Fig. 2a–b), with the exception of orebody III_3 that occurs in the monzonite porphyry. Six ore blocks (containing 21 orebodies) have been delineated, among which the I, III and IV ore blocks (with 13 orebodies) are currently mined.

Chalcopyrite and pyrrhotite occur as veinlets, disseminated or locally as massive (Fig. 4g–j) within coarse quartz-calcite vein or skarn. Quartz-calcite-sulfide vein is the main (> 90%) ore type at Langdu, and the calcite in these ore veins is denoted as type-II (Fig. 4i). Near the wall rock, calcite-sulfide veins infill in the marble or limestone. This calcite is denoted as type-III. Sphalerite, scheelite, native bismuth, and kawazulite occur as anhedral inclusions within the chalcopyrite or pyrrhotite (Fig. 5j–i).

4. Sampling and analytical methods

Eleven chalcopyrite and nine pyrrhotite samples from the Langdu deposit were selected for the sulfur isotope analysis using a Finnigan MAT-251 mass spectrometer, which was performed at the State Key Laboratory of Environmental Geochemistry (SKLEG), Institute of Geochemistry, Chinese Academy of Sciences (IGCAS). Analytical procedures are described by Ueda and Sakai (1984), with an overall analytical precision of ± 0.2‰ for $\delta^{34}S_{CDT}$.

Thirteen calcite samples were collected from mine tunnels of the Langdu deposit. As above-mentioned, the calcites can be classified into type-I,-II and -III. Type-I calcite is white and occurs as fracture-infills in pyroxene and garnet (Fig. 4f). Type-II calcite is generally milky-white and associated with quartz, pyrrhotite and chalcopyrite (Fig. 4i). Type-

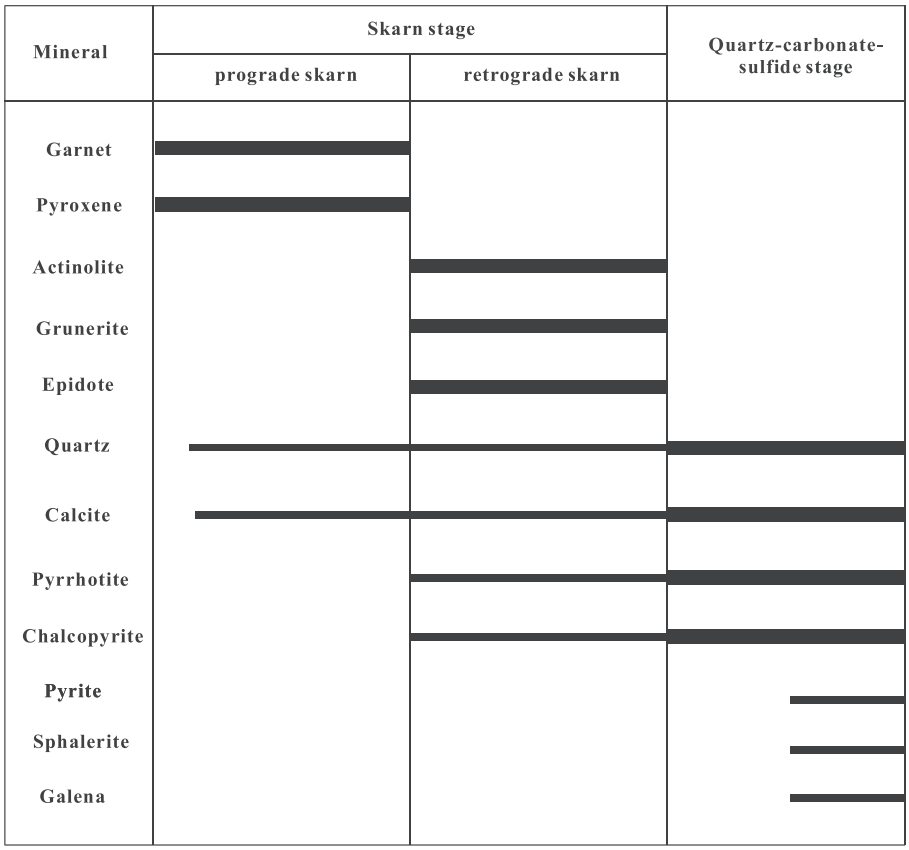

Fig. 3. Paragenetic sequence of various minerals in the Langdu deposit.

III calcite is separated from coarse calcite-chalcopyrite veins. Carbon-oxygen isotopic compositions of the calcites were determined with the method described by McCrea (1950) and Rosenbaum and Sheppard (1986), also at the SKLEG. Isotopic analysis of the prepared CO_2 gas samples was performed with a Finnigan MAT-253 mass spectrometer, with an overall analytical precision of ± 0.2‰ for $\delta^{13}C_{PDB}$ and $\delta^{18}O_{SMOW}$.

Six quartz, one garnet, three pyroxene, one chlorite and one biotite samples were collected from the Langdu deposit for the oxygen isotope analysis. The biotite sample was taken from an altered monzonite porphyry. The gray-green euhedral pyroxene and reddish-brown garnet samples were taken from the sulfide-bearing skarn. All of the quartz samples were taken from the coarse-grained sulfide-quartz veins. A chlorite sample was taken from a chlorite-calcite-sulfide vein. Oxygen isotope analysis was performed at the Institute of Mineral Resources, Chinese Academy of Geological Sciences (Beijing), using a Finnigan MAT-253 mass spectrometer and following the methods of Clayton and Mayeda (1963) and Borthwick and Harmon (1982).

Quartz samples for the fluid inclusion (FI) microanalysis were collected from mine tunnels at Langdu. Primary FIs are abundant in sulfide-bearing quartz, but are absent in the skarn minerals. Based on the phase relationships at room temperature and the phase transitions during heating and cooling (Roedder, 1984; Lu et al., 2004), we recognize four types of FIs: aqueous two phase (type-I), vapor-rich methane-nitrogen (type-II), single phase methane-nitrogen (type-III), and daughter-mineral-bearing (type-IV). The aqueous two phase FIs can be further subdivided into three sub-types, i.e., liquid-rich (type-Ia), methane-bearing (type-Ib), and $CaCl_2$-bearing (type-Ic) FIs.

Fluid inclusion studies were conducted at the State Key Laboratory of Ore Deposit Geochemistry (SKLODG), IGCAS. The sulfide-bearing quartz samples were sliced and polished to ~200 μm thick for FI petrographic observation and the subsequent microthermometric analyses. The latter was performed with a Linkam THMSG600 heating-freezing stage with a temperature range of −196 to 600 °C, which was calibrated with synthetic inclusions. The temperature measurements have an uncertainty of ± 0.2 °C for temperatures between −60 and 100 °C, ± 0.5 to ± 2 °C between −60 and −120 °C, ± 3 °C between −120 and −190 °C, and ± 2 °C for temperatures > 100 °C.

Qualitative determinations of the FI compositions were conducted using a Renishaw 1000 laser Raman microspectrometer at the SKLODG with a 514-nm Ar-ion laser. Salinities of aqueous FIs were calculated from their final ice-melting temperature with the equation of Bodnar (1993). Salinities of daughter-mineral-bearing FIs were calculated with the equation of Hall et al. (1988), whilst those of the H_2O-NaCl-$CaCl_2$ FIs were calculated with the equation of Chi and Ni (2007).

5. Results

5.1. Fluid inclusions

5.1.1. Fluid inclusion petrography

The liquid-rich two phase FIs are the most abundant in the quartz samples. Type-I FIs occur in isolation or as clusters, and 2–30 vol% is occupied by bubbles. These FIs are usually 3–21 μm in size (Fig. 7a–b), and are elliptical, elongated, negative-crystal or irregularly-shaped.

Type-II FIs are typically elliptical or rounded, 5–15 μm in size, and are spatially associated with type-IV FIs (Fig. 7c–d).

Type-III FIs occur in isolation or clusters, and are 5–15 μm in size (Fig. 7e–j).

Type-IV FIs contain a vapor bubble, a brine liquid, and a cubic transparent blue solid. The FIs are 5–20 μm in size, and are rounded, elongated, or irregularly-shaped (Fig. 7c–d).

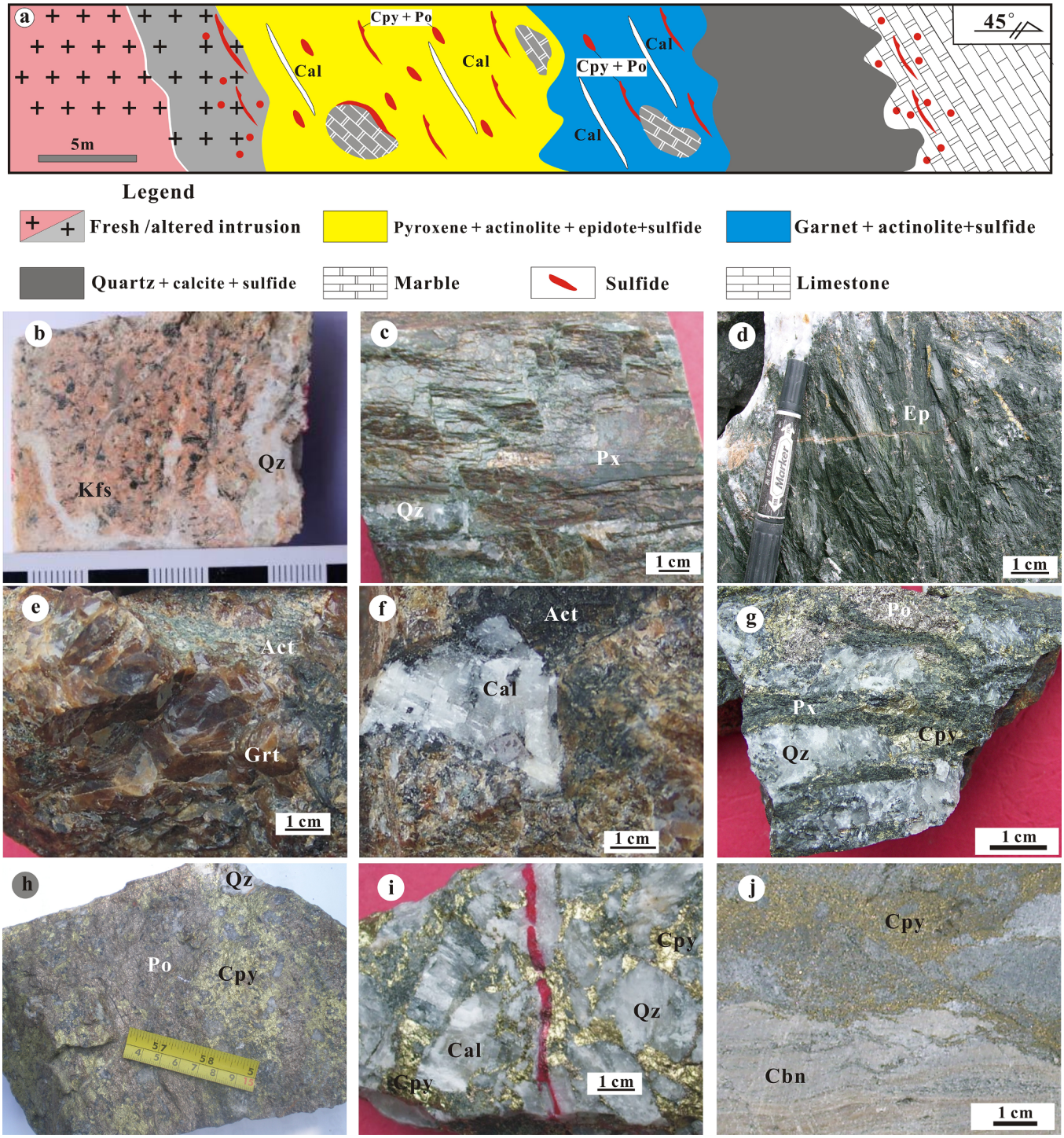

Fig. 4. (a) Simplified geologic sketch map of Langdu deposit. (b) Secondary K-feldspar clusters with fine-grained biotite. (c) Green tabular pyroxene. (d) Radial epidote clusters. (e) Reddish- brown idiomorphic garnet partly replaced by actinolite (disseminated chalcopyrite locally observed). (f) Calcite infilling cavities in reddish-brown idiomorphic garnet. (g) Intergrowth of chalcopyrite, quartz and pyrrhotite in pyroxene. (h) Massive sulfide ore. (i) Coarse chalcopyrite-bearing calcite-quartz vein. (j) Disseminated chalcopyrite in limestone. Abbreviations: Kfs = K-feldspar; Grt = garnet; Px = pyroxene; Qz = quartz; Cal = calcite; Act = actinolite; Cpy = chalcopyrite; Po = pyrrhotite; Cbn = carbonate; Ep = epidote. (For interpretation of the references to colour in this figure legend, the reader is referred to the web version of this article.)

5.1.2. Microthermometric results

Type-I liquid-rich two-phase FIs

Homogenization temperatures (T_h) and ice-melting temperatures (T_m) of type-Ia FIs are of 110–266 °C (Table 3; Fig. 8a) and −5.1 to −1.0 °C, respectively, and calculated salinities of 1.7–8.0 wt% NaCl eqv. (Table 3; Fig. 8b).

Type-Ib FIs contain 20–30% bubbles (Fig. 8b). Raman spectrometry indicates that the bubbles contain methane, yet we did not observe clathrate during cooling. The homogenization temperatures of the type-Ib FIs are of 203–338 °C (Table 3; Fig. 8a).

The eutectic temperatures of type-Ic FIs are of −76.3 to −52.0 °C (Table 3), consistent with a H_2O-NaCl-$CaCl_2$ system (Roedder, 1984). Their ice-melting temperatures are of −43.3 to −21.9 °C and hydrohalite/clathrate melting temperatures (T_{m-HH}) were not observed. Chi

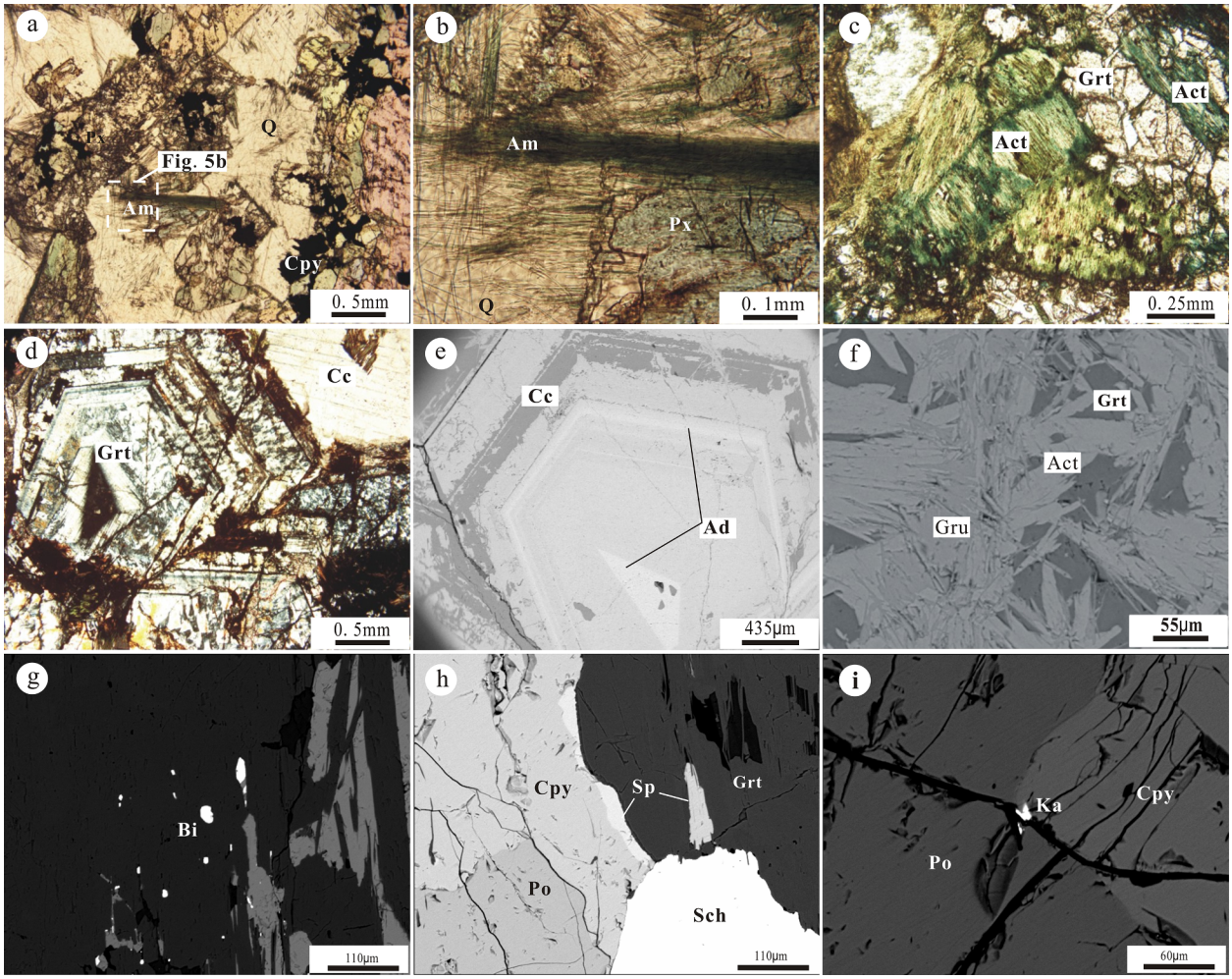

Fig. 5. Photomicrographs and backscattered electron (BSE) images of minerals. (a) Pyroxene partly replaced or fragmented by quartz, actinolite or chalcopyrite (plane polarized light). (b) Fibrous actinolite grown with quartz (plane polarized light). (c) Euhedral garnet partly replaced by actinolite (plane polarized light). (d) Coarse-grained garnet with compositional zoning (cross polarized light). Darker core are more andraditic than lighter bands. (e) BSE image of coarse-grained garnet, with some compositional bands. (f) BSE image of radiating amphibole clusters. Dark mineral is grunerite and lighter one is actinolite. (g) Star-like bismuth in skarn. (h) Intergrowth of chalcopyrite, pyrrhotite, sphalerite and scheelite in the ore. (i) Kawazulite as anhedral inclusions in sulfides. Abbreviations: Grt = garnet; Px = pyroxene; Am = amphibole; Cpy = chalcopyrite; Cc = calcite; Ad = andradite; Gru = grunerite; Act = actinolite; Po = pyrrhotite; Sp = sphalerite; Sch = scheelite; Ka = kawazulite; Bi = bismuth.

Table 1
Representative EPMA data (wt. %) of pyroxene in the Langdu deposit.

Sample No	LD19-01	LD19-02	LD19-03	LD1502-1	LD1502-02	LD1502-03	LD1502-06	LD1902-05	LD1902-06	LD1902-07
Na_2O	0.07	0.08	0.08	0.06	0.06	0.11	0.11	0.05	0.04	0.04
MgO	1.26	1.42	1.17	1.77	1.06	1.24	0.79	1.19	1.11	0.52
Al_2O_3	0.01	0.01	0.01	0.04	0.05	0.22	0.04	0.04	0.11	0.00
SiO_2	49.16	49.40	49.40	49.52	48.62	49.14	49.10	49.38	48.86	48.74
CaO	23.26	23.09	22.89	22.04	22.77	22.76	23.00	22.99	22.97	23.08
FeO	24.63	23.10	24.37	22.59	24.32	23.77	25.01	24.23	24.72	25.49
MnO	1.38	2.02	1.33	3.16	2.11	2.51	1.45	1.45	1.47	1.29
Total	99.77	99.12	99.25	99.18	98.99	99.75	99.50	99.33	99.28	99.16
Cations based on 6 oxygens										
Na	0.01	0.01	0.01	0.00	0.01	0.01	0.01	0.00	0.00	0.00
Mg	0.08	0.09	0.07	0.11	0.07	0.08	0.05	0.07	0.07	0.03
Al	0.00	0.00	0.00	0.00	0.00	0.02	0.00	0.00	0.01	0.00
Si	2.01	2.03	2.03	2.03	2.01	2.01	2.02	2.03	2.01	2.02
Ca	1.02	1.02	1.01	0.97	1.01	1.00	1.01	1.01	1.01	1.02
Fe	0.84	0.79	0.84	0.77	0.84	0.81	0.86	0.83	0.85	0.88
Mn	0.05	0.07	0.05	0.11	0.07	0.09	0.05	0.05	0.05	0.05
Mole percent										
Diopside	8.03	9.21	7.54	11.01	6.74	7.82	5.08	7.70	7.08	3.35
Johannsenite	4.94	7.38	4.86	11.05	7.53	8.91	5.25	5.29	5.28	4.71
Hedenbergite	87.03	83.40	87.60	77.94	85.73	83.27	89.67	87.01	87.64	91.94

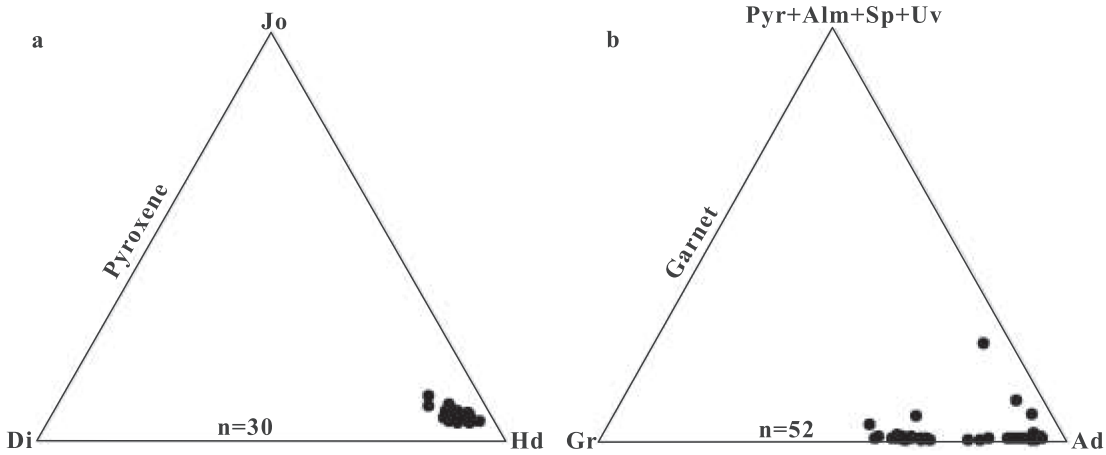

Fig. 6. Ternary plots of pyroxene and garnet compositions from the Langdu deposit. Abbreviations: Jo = johannsenite; Di = diopside; Hd = hedenbergite; Ad = andradite; Gr = grossularite; Alm = almandine; Sp = spessartine; Pyr = pyralspite; Uv = uvarovite.

Table 2
Representative EPMA data (wt. %) of garnet in the Langdu deposit.

Sample No	LD4102-11	LD4102-12	LD4102-13	LD4302-08	LD4302-09	LD4302-10	LD4302-11	LD44-08	LD44-09
SiO_2	37.09	37.16	36.83	37.31	37.17	36.25	36.89	36.28	36.10
TiO_2	0.01	0.00	0.00	0.00	0.01	0.01	0.07	0.00	0.02
Al_2O_3	7.58	6.56	5.99	7.65	6.89	0.00	6.32	0.00	0.90
Fe_2O_3	19.50	20.94	21.82	19.46	20.72	30.17	21.63	29.73	28.09
MnO	0.40	0.38	0.49	0.45	0.39	0.17	0.22	0.23	0.20
MgO	0.01	0.09	0.02	0.02	0.01	0.04	0.01	0.01	0.04
CaO	34.86	34.69	34.49	34.47	34.42	33.70	35.04	33.67	33.69
Total	99.45	99.82	99.64	99.36	99.61	100.34	100.18	99.92	99.04
Cations based on 24 oxygens									
Si	3.05	3.04	3.25	3.06	3.30	2.82	3.23	3.02	3.04
Ti	0.00	0.00	0.00	0.00	0.00	0.00	0.00	0.00	0.00
Al	0.64	0.58	0.00	0.67	0.00	0.58	0.04	0.09	0.12
Fe	1.21	1.29	1.45	1.20	1.39	1.77	1.42	1.86	1.78
Mn	0.03	0.03	0.04	0.03	0.03	0.01	0.02	0.02	0.01
Mg	0.00	0.01	0.00	0.00	0.00	0.00	0.00	0.00	0.00
Ca	3.07	3.04	3.26	3.03	3.28	2.81	3.29	3.00	3.04
Mole percent									
Uvarovite	0.00	0.36	0.05	0.00	0.00	0.00	0.00	0.02	0.13
Andradite	58.38	62.80	65.87	58.81	62.84	93.81	64.69	92.47	87.30
Almandine	0.00	0.00	0.00	0.00	0.00	0.00	0.00	0.00	0.00
Spessartine	0.89	0.86	1.10	1.01	0.88	0.38	0.49	0.54	0.47
Pyralspite	0.05	0.37	0.08	0.09	0.04	0.16	0.03	0.05	0.16
Grossularite	40.68	35.61	32.90	40.08	36.24	5.65	34.79	6.92	11.95

and Ni (2007) suggested that T_{m-ice} can represent the maximum T_{m-HH}. Salinities of the type-Ic FIs are therefore calculated from their T_{m-ice} following the method of Chi and Ni (2007), which yielded 23.3–29.5 wt % NaCl + $CaCl_2$ eqv. (Table 3; Fig. 8b) and Ca/Na molar ratios of 0.1–5.7. All of the type-Ic FIs homogenized at 129–333 °C (Table 3; Fig. 8a).

Type-II vapor-rich methane-nitrogen FIs

Type-II FIs homogenized to a vapor phase or decrepitated before the homogenization (Fig. 5c, d). Methane-nitrogen mixed bubbles separated into a liquid and a vapor phase when cooled to −90 °C. The vapor homogenized at −87.5 to −83.7 °C (Table 3), which is below the critical point for pure methane (−82.6 °C; Van den Kerkhof and Thiéry, 2001). Their final homogenization temperatures range from 262 to 425 °C (Table 3; Fig. 8a).

Type-III single phase methane-nitrogen FIs

A vapor phase was observed at below −120 °C (Fig. 7h, i), and it increased in size with decreasing temperature. Solid phase was not observed, even at temperatures below −190 °C. The vapor homogenized to a liquid phase at −117 to −114 °C (Table 3; Fig. 5g–j and 8a). The homogenization temperatures of the type-III FIs are also below the critical point of pure CH_4 (−82.6 °C; Van den Kerkhof and Thiéry, 2001).

Type-IV daughter mineral-bearing FIs

Type-IV FIs homogenized after the dissolution of halite at 295–392 °C (Table 3; Fig. 8a), with correspondingly salinities of 37.8–46.6 wt% NaCl eqv. (Table 3; Fig. 8b).

5.1.3. Laser Raman spectroscopy

Laser Raman spectroscopy reveals that the vapor phase of type Ia, Ic and IV and liquid phase of type I, type II and IV FIs are dominantly pure H_2O. While CH_4 is identified in vapor phase of type-Ib and type II FIs (Fig. 9a–b). Type III FIs yielded an apparent signal at ~2912 cm^{-1} and a week signal at ~2325 cm^{-1} coincided with the CH_4 and N_2, respectively (Fig. 9c–d).

5.2. Sulfur, carbon and oxygen isotopic compositions

$\delta^{34}S_{CDT}$ values of the sulfide minerals are given in Table 4 and shown in Fig. 10. $\delta^{34}S_{CDT}$ values of chalcopyrite and pyrrhotite are of −5.3 to 0.7‰ and −1.0 to 0.7‰, respectively.

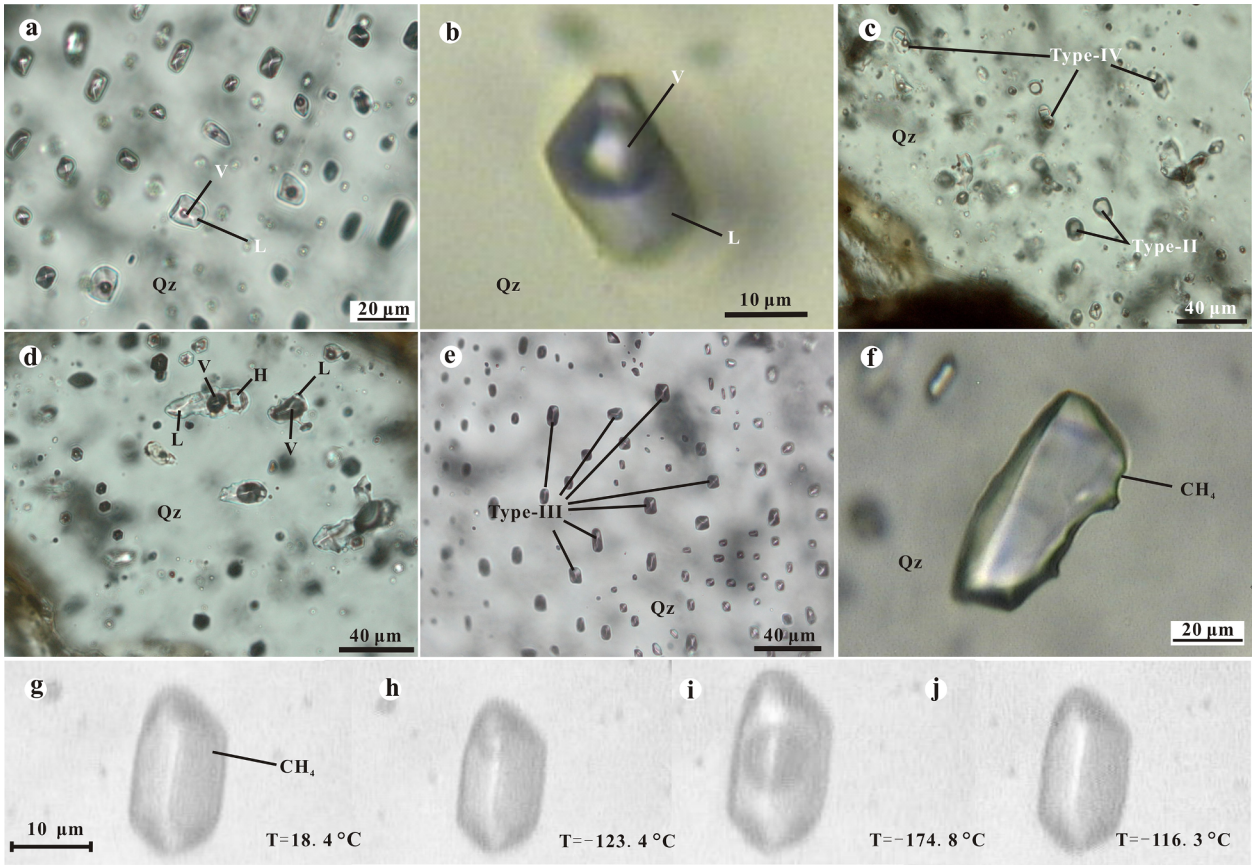

Fig. 7. Fluid inclusions in quartz. (a) clustered liquid-rich (type-I) FIs; (b) methane-bearing aqueous FIs (type-II) containing a moderately large vapor bubble; (c) and (d) coexisting daughter mineral (halite-bearing), single phase/vapor-rich methane-nitrogen FIs; (e) clustered and (f) isolated single phase methane-nitrogen FIs; (g–j) Low-temperature phase transition of single phase methane-nitrogen FIs (type-III). Abbreviations: Qz = Quartz; V = vapor; L = liquid; H = halite.

$\delta^{13}C_{PDB}$ values of the type-I and -II calcites are of −8.4 to −6.1‰ (Table 5), and their $\delta^{18}O_{SMOW}$ values are of 10.1 to 13.0‰. Type-III calcite has $\delta^{13}C_{PDB}$ and $\delta^{18}O_{SMOW}$ values of −5.6 to 0.2‰ and 12.5 to16.3‰, respectively (Table 5; Fig. 11).

Biotite, garnet, pyroxene, quartz, and chlorite have $\delta^{18}O_{SMOW}$ values of 6.9‰, 4.1‰, 5.5–7.5‰, 13.2–15.3‰, and 6.8‰, respectively (Table 5; Fig. 12).

6. Discussion

6.1. Origin of the ore-forming fluids

The $\delta^{18}O_{SMOW}$ values of ore-forming fluids from the Langdu deposit are calculated based on $\delta^{18}O_{SMOW}$ values of hydrothermal minerals at different temperatures. The isotope fractionation equations of Zheng (1993a,b) were used for secondary biotite, pyroxene, garnet, and quartz, the equation of Cole and Ripley (1999) for chlorite, and the equation of O'Neil et al. (1969) for calcite.

Formation temperatures of secondary biotite in the altered porphyries were assumed to be around 500 to 600 °C (Hedenquist et al., 1998). The calculated $\delta^{18}O_{SMOW}$ values of the hydrothermal fluids in equilibrium with the secondary biotite are of 9.3 to 9.4‰ (Table 5), which fall in the magmatic fluid field (Taylor, 1979). Coexistence of type-II and -IV FIs with similar homogenization temperatures in quartz veins indicates that these FIs were possibly trapped in a fluid immiscibility system (e.g., Roedder, 1984; Baker and Lang, 2003). Previous studies suggested that homogenization temperatures can represent the formation temperatures of host minerals in immiscibility (e.g., Roedder, 1984; Lu et al., 2004). We therefore assume that the skarn minerals, quartz, and type-I and -II calcite were formed at 300–400 °C, falling within the homogenization temperature range of the type-II and -IV FIs. The $\delta^{18}O_{SMOW}$ values were also calculated for

Table 3
Microthermometric data of fluid inclusions in the Langdu deposit.

Type of fluid inclusion	Host Mineral	T_h CH_4 (°C)	T_e (°C)	$T_{s(hal)}$ (°C)	T_h (°C)	Salinity (wt. % NaCl ± $CaCl_2$ eqv.)
Type Ia	Quartz	–	–	–	110 to 266	1.7 to 8.0
Type Ib	Quartz	–	–	–	203 to 338	–
Type Ic	Quartz	–	−76.3 to −52.0	–	129 to 333	23.3 to 29.5
Type II	Quartz	−87.5 to −83.7	–	–	262 to 425	–
Type III	Quartz	–	–	–	−117 to −114	–
Type IV	Quartz	–	–	295 to 392	295 to 392	37.8 to 46.6

Abbreviations: T_h CH_4 = homogenization temperature of CH_4, T_e = eutectic temperature, $T_{s\ (hal)}$ = dissolution temperature of halite, T_h = homogenization temperature.
Unit of salinity for type Ic inclusion is written as wt. % NaCl + $CaCl_2$ eqv.

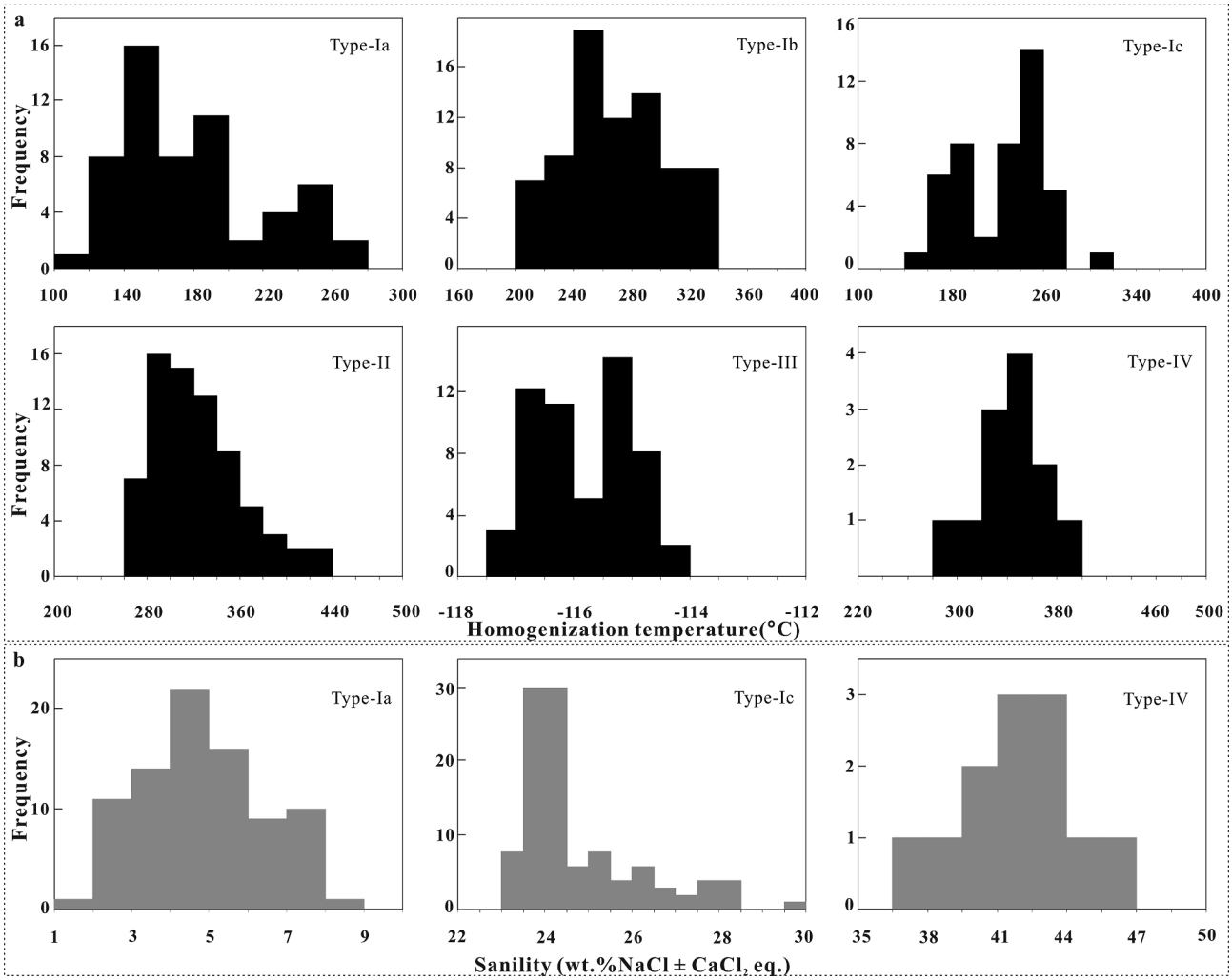

Fig. 8. Histograms of homogenization temperatures (a) and salinities (b) of FIs in the Langdu deposit. Unit of salinity for type Ic FIs is expressed as wt. % NaCl + $CaCl_2$ eqv.

the fluids in equilibrium with garnet and pyroxene (5.7–8.9‰), quartz (6.2–10.8‰), and calcite (5.0–10.2‰; Table 5; Fig. 12). Majority of the calculated $\delta^{18}O_{SMOW}$ values for garnet, pyroxene, quartz, and calcite also fall in the magmatic fluid field (Table 5; Fig. 12). The main homogenization temperature range (150–200 °C) of type-Ia FIs from the chlorite-calcite-bearing quartz veins was used to calculate the $\delta^{18}O_{SMOW}$ of the ore-forming fluids in equilibrium with chlorite and type-III calcite (Table 5; Fig. 12). The results suggest that meteoric/formation water was involved in the mineralization. This interpretation is also supported by the sulfur isotopic data of the sulfides, which fall into two main clusters in the histogram (Fig. 10): one (−1.1 to +0.7‰) with magmatic affinity (−3 to +3‰) and the other (−5.3 to −4.6‰) with biogenic affinity, implying that organic-rich sedimentary rocks may also have supplied some sulfur. The carbon and oxygen isotope compositions of the various calcites indicate a similar ore-forming fluids evolution trend. Type-III calcite has higher ^{13}C and ^{18}O compositions than type-II calcite (Table 5). And $\delta^{13}C_{PDB}$ and $\delta^{18}O_{SMOW}$ values of the type-II calcite are also higher than those of the type-I calcite. In the $\delta^{13}C_{PDB}$ vs. $\delta^{18}O_{SMOW}$ plot (Fig. 11), the majority of the samples fall within or near the carbonatites field. The higher $\delta^{13}C_{PDB}$ and $\delta^{18}O_{SMOW}$ of type-III calcite than type-I calcite (Fig. 11) suggest that the original isotopic signatures of the limestone were modified by mixing with isotopically depleted hydrothermal fluids. The varying $\delta^{13}C_{PDB}$ and $\delta^{18}O_{SMOW}$ may thus reflect different water/rock ratios.

6.2. Ore-forming fluids evolution

Petrographic and microthermometric studies of the FIs indicate four types hydrothermal fluids at Langdu, including: high temperature and high salinity fluids, and high temperature, low salinity, and CH_4-rich fluids (fluid 3 and 4 to be described below). The two distinct types of fluids were likely formed by immiscibility during which volatiles were separated as a vapor phase to form the high temperature, low salinity and CH_4-rich fluids, and sodium remained in the residual brine to form the high temperature and high salinity fluids. Previous studies demonstrate that methane can be incorporated into ore-forming fluids via four paths: (1) biogenic activities; (2) Fischer-Tropsch synthesis; (3) reaction with carbonate wallrocks; and (4) exsolution from the melt (Salvi and Williams-Jones, 1997; Potter and Konnerup-Madsen, 2003; Etiope and Sherwood Lollar, 2013; Zhang et al., 2019). Homogenization temperatures of the Langdu FIs (mostly 200–400 °C) may have been too high for bacterial activities, but far below the necessary temperature of the Fischer-Tropsch synthesis. No direct geological or geochemical evidences for magmatic-generated methane are found in this study. Thus, the CH_4 in ore-forming fluids at Langdu was most likely derived from the fluids-carbonaceous wallrock interactions, as expressed in the formula: $2C + 2H_2O \rightarrow CH_4 + CO_2$ (Wang et al., 2008a). This conclusion supported by the intensive and extensive contact metasomatism and the identification of carbonaceous material in quartz crystals by Raman spectroscopy.

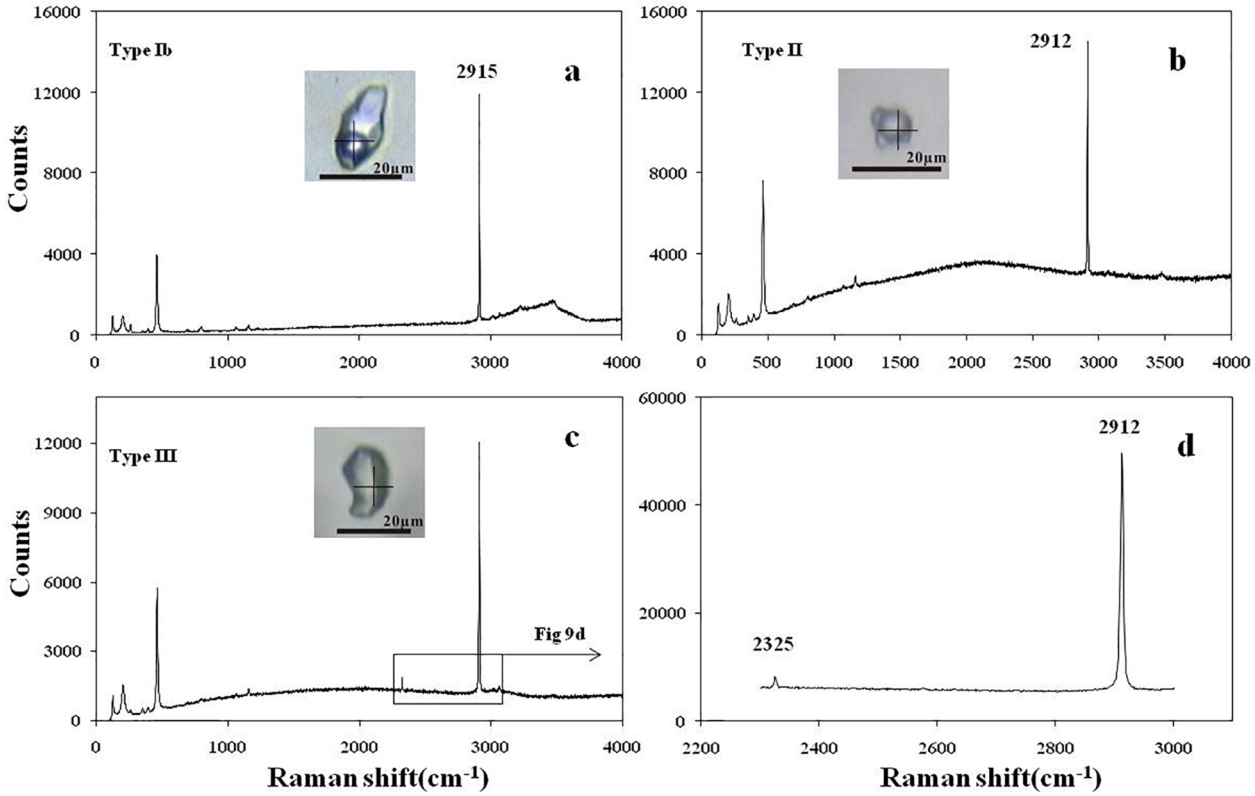

Fig. 9. Laser Raman spectroscopy of FIs in quartz.

Table 4
Sulfur isotope data of sulfides in the Langdu deposit.

Sample No	Measured $\delta^{34}S_{CDT}$(‰)	
	Pyrrhotite	Chalcopyrite
LD0820	0.1	–
LD0823	0.2	–
LD0807	0.7	0.7
LD0824	0.6	0.6
LD0818	0.4	0.4
LD0822	0.4	0.6
LD0811	–	0.6
LD0757	–	−1.1
LD0760	–	−5.3
LD0774	–	−4.6
LD0759	–	−5.3
LD0763	−1.0	–
LD0767	−0.7	–
LD07101	−0.9	–
LD0773	–	−4.9
LD0777	–	−4.9

The third type of fluid is intermediate temperature, high salinity and $CaCl_2$-bearing fluids. Such H_2O-NaCl-$CaCl_2$ fluids may reflect Ca^{2+} release and calc-silicate deposition during skarn formation (Kwak and Tan, 1981). Eutectic temperatures of the $CaCl_2$-rich FIs measured in this study are mostly below those of pure H_2O-NaCl-$CaCl_2$ aqueous solution (−52 °C), reflecting the influence of metastable $CaCl_2$ hydrates (Davis et al., 1990) or that of a polysaline brine (i.e., $FeCl_2$-, $MgCl_2$-, or KCl-bearing; Ruano et al., 2002; Lu et al., 2004). The fourth type of fluid is a low temperature and low salinity fluids, which may reflect mixing of magmatic fluid and meteoric/formation water during fluid ascent or migration.

6.3. Sulfide deposition and causes of high-grade Cu mineralization

The Langdu deposit shares similar features of ore mineralogy, elemental geochemistry, stable isotopes, and FI geothermometry to those of typical Cu skarn deposits. And our discussion above shows that the Langdu ore-forming fluids derive from magma, which typically has high concentrations of ore-metals (e.g., Cu, Fe, Zn, Pb) and volatiles (Wen et al., 2019). During the fluid immiscibility, the volatiles may have degassed, concentrating the Cu (in chloride complexes) in the residual brine phase. Supersaturation of the brine with metals may have triggered the sulfide deposition. The subsequent pressure-temperature drop and pH increase (neutralization) led by the meteoric/formation water incursion may have formed the sulfide-quartz-calcite veins. There is no doubt that formation of high-grade Cu ore in Langdu deposit may be coupling interaction of extensive fluids/wallrock reaction, fluid mixing and present of methane.

Although CH_4-bearing FIs have been identified in various types of hydrothermal deposit, such as Changba VMS Pb–Zn deposit in Gansu, Hongshan skarn Cu deposit in NW Yunnan, 17 Mile Hill deposit in Australia and Copper Canyon deposit in USA (e.g., Rowins, 2000; Wang et al., 2008b; Guo et al., 2009; Peng et al., 2016; Zhang et al., 2019). Most of them contain very low contents of CH_4 or just a few CH_4-rich FIs. Langdu deposit contains not only a large number of CH_4-bearing FIs, but also abundant CH_4-rich and single-phase CH_4 FIs. These deposits have two common features: (1) high ore grade, such as the deposit of Langdu (average > 6% Cu), Changba (average > 20% Pb + Zn) and Hongshan (average 1.7% Cu, 9.0% Pb + Zn); (2) pyrrhotite is common. CH_4 plays a key metallogenic role in these deposits, this paper tentatively summarizes the following two functions: (1) Facilitating fluid immiscibility. Previous studies suggested that gas mixture has much less soluble than their pure end-members (Naden and Shepherd, 1989). Therefore, the presence of both CH_4 and N_2 in hydrothermal fluids can greatly expand the temperature-pressure field of vapor/liquid immiscibility. This means that the extent at which phase

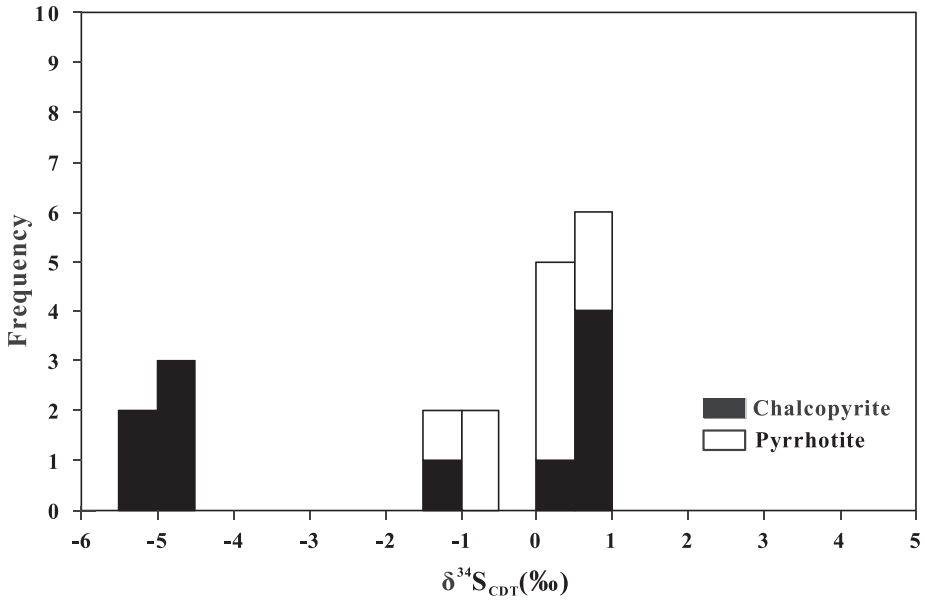

Fig. 10. Sulfur isotope histogram for the chalcopyrite and pyrrhotite from Langdu.

Table 5
Measured oxygen and carbon isotope data and calculated isotopic compositions of equilibrium water.

Sample	Mineral	Measured(‰)		Calculated $\delta^{18}O_{SMOW}$ water composition (‰)					
		$\delta^{18}O_{SMOW}$	$\delta^{13}C_{PDB}$	600 °C	500 °C	400 °C	300 °C	200 °C	150 °C
LD07131	Biotite	6.9	–	9.4	9.3			–	–
LD0844	Garnet	4.1	–	–	–	7.0	6.2	–	–
LD0843	Pyroxene	7.5	–	–	–	8.9	7.7	–	–
LD0706	Pyroxene	5.5	–	–	–	6.9	5.7	–	–
LD0815	Pyroxene	6.9	–	–	–	8.3	7.1	–	–
LD 0773	Quartz	15.3	–	–	–	10.8	8.3	–	–
LD 0787	Quartz	14.7	–	–	–	10.2	7.7	–	–
LD0812	Quartz	13.3	–	–	–	8.8	6.3	–	–
LD0750	Quartz	14.0	–	–	–	9.5	7.0	–	–
LD0756	Quartz	13.2	–	–	–	8.7	6.2	–	–
LD0779	Quartz	14.9	–	–	–	10.4	7.9	–	–
LD0707	Type I Calcite	10.1	−7.8	–	–	7.3	5.0	–	–
LD0819	Type I Calcite	10.2	−8.3	–	–	7.5	5.2	–	–
LD0815	Type I Calcite	12.3	−8.4	–	–	9.5	7.2	–	–
LD0754	Type II Calcite	12.2	−6.2	–	–	9.5	7.2	–	–
LD0749	Type II Calcite	12.0	−6.3	–	–	9.3	6.9	–	–
LD0791	Type II Calcite	13.0	−6.1	–	–	10.2	7.9	–	–
LD0790	Type II Calcite	12.5	−6.3	–	–	9.8	7.4	–	–
LD0780	Type III Calcite	13.2	−1.8	–	–	–	–	4.2	1.1
LD0718	Type III Calcite	12.5	−2.1	–	–	–	–	3.4	0.3
LD0787	Type III Calcite	12.5	−5.6	–	–	–	–	3.4	0.3
LD0788	Type III Calcite	16.3	0.2	–	–	–	–	7.2	4.1
LD0785	Type III Calcite	15.2	−1.1	–	–	–	–	6.2	3.0
LD078802	Type III Calcite	14.3	−0.2	–	–	–	–	5.2	2.1
LD0780	Chlorite	6.8		–	–		–	3.4	–

separation can happen will be greatly enlarged. (2) Reduced the sulfates (SO_4^{2-}) to sulfides (S^{2-}) by the following reaction: $CH_4 + SO_4^{2-} \rightarrow S^{2-} + CO_2 + 2H_2O$ (Heydari and Moore, 1989). Pyrrhotite, rather than pyrite, occurring in the ore suggests that the metallogenic condition is an anomalously reducing environment (Meinert, 1982; Peng et al., 2016).

7. Conclusions

1. The Langdu Cu skarn mineralization was related to magmatic intrusion into the Qigasi Fm. Stable isotope compositions of the Langdu ore-forming fluids suggest a magmatic source, and that the magmatic fluids were contaminated by meteoric/formation water. Large amounts of CH_4 and N_2 were likely incorporated into the ore-forming fluids when the magmatic fluids reacted with the carbonaceous slates.
2. Established the mechanism of ore formation in the Langdu deposit. Methane played a critical role in the formation of high-grade Cu ores in the Langdu deposit, as it expanded the pressure-temperature field of vapor/liquid immiscibility, and significantly reduced the oxygen fugacity. Formation of high-grade Cu ore at Langdu deposit may be coupling of CH_4, extensive water/rock reaction and fluid mixing.

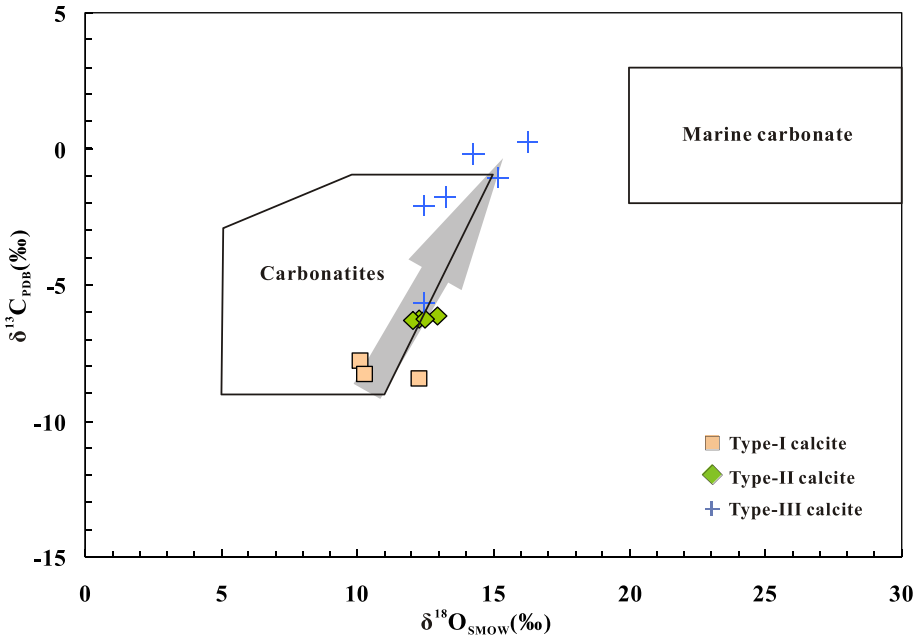

Fig. 11. Carbon and oxygen isotope diagram for the calcites from the Langdu skarn copper deposit. fields of carbonatites and marine carbonate are after Ray et al. (2000) and Zheng (2001), respectively.

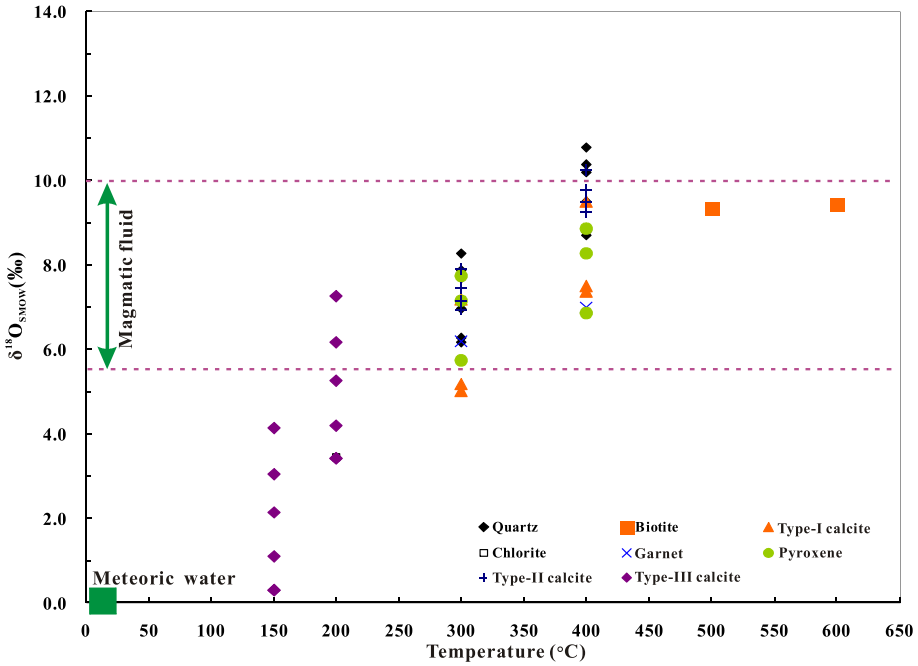

Fig. 12. Plot of calculated oxygen isotopic compositions of ore-forming fluids based on measured oxygen isotopic compositions of biotite, andradite, hedenbergite, quartz, calcite and chlorite. The ranges of oxygen isotopic compositions of magmatic fluid and meteoric water are from Taylor (1979) and Sheppard (1986).

Declaration of Competing Interest

The authors declare that they have no known competing financial interests or personal relationships that could have appeared to influence the work reported in this paper.

Acknowledgements

This study was jointly supported by the National Key R&D Program of China (2016YFC0600405) and the National Natural Science Foundation of China (41425011, 41203039 and U1133602). The authors wish to thank C. Z. Yang (Branch of Mineral Resources Investigation, Yunnan Geological Survey) for useful help.

References

Baker, T., Lang, J.R., 2003. Reconciling fluid inclusion types, fluid processes, and fluid sources in skarns: an example from the Bismark Deposit. Mexico. Miner. Deposita 38, 474–495.

Bodnar, R.J., 1993. Revised equation and table for determining the freezing point depression of H_2O-NaCl solutions. Geochim. Cosmochim. Acta 57, 683–684.

Borthwick, J., Harmon, R.S., 1982. A note regarding ClF_3 as an alternative to Br $_F$3 for oxygen isotope analysis. Geochim. Cosmochim. Acta 46 (9), 1665–1668.

Chi, G.X., Ni, P., 2007. Equations for calculation of NaCl/(NaCl + $CaCl_2$) ratios and salinities from hydrohalite-melting and ice-melting temperatures in the H_2O-NaCl-$CaCl_2$ system. Acta Petrol. Sin. 23 (1), 33–37.

Clayton, R.N., Mayeda, T.K., 1963. The use of bromine pentafluoride in the extraction of oxygen from oxides and silicates for isotopic analysis. Geochim. Cosmochim. Acta 27 (1), 43–52.
Cole, D.R., Ripley, E.M., 1999. Oxygen isotope fractionation between chlorite and water from 170°C to 350°C: a preliminary assessment based on partial exchange and fluid/rock experiments. Geochim. Cosmochim. Acta 63 (3–4), 449–457.
Davis, D.W., Lowenstein, T.K., Spencer, R.J., 1990. Melting behavior of fluid inclusions in laboratory-grown halite crystals in the systems NaCl-H_2O, NaCl-KCl-H_2O, NaCl-$MgCl_2$-H_2O, and NaCl-$CaCl_2$-H_2O. Geochim. Cosmochim. Acta 54 (3), 591–601.
Etiope, G., Sherwood Lollar, B., 2013. Abiotic methane on earth. Rev. Geophys. 51 (2), 276–299.
Guo, J.H., Leng, C.B., Zhang, X.C., Zafar, T., Chen, W.T., Zhang, W., Tian, Z.D., Tian, P., Lai, C.K., 2020... Textural and chemical variations of magnetite from porphyry Cu–Au and Cu skarn deposits in the Zhongdian region, northwestern, Yunnan, SW China. Ore Geol. Rev. 116, 103245.
Guo, L.J., Xie, Y.L., Hou, Z.Q., Wang, S., Chen, W., Li, Z., Li, Y.X., Xue, H.M., Tong, Y., Pan, X.F., Zhou, X.W., 2009. Geology and ore fluid characteristics of the Bairendaba silver polymetallic deposit in Inner Mongolia. Acta Petrol. Miner. 28 (1), 26–36 (in Chinese with English abstract).
Hall, D.L., Sterner, S.M., Bodnar, R.J., 1988. Freezing point depression of NaCl-KCl-H_2O solutions. Econ. Geo. 83 (1), 197–202.
Hedenquist, J.W., Arribas, A., Reynolds, T.J., 1998. Evolution of an intrusion-centered hydrothermal system: far Southeast-Lepanto porphyry and epithermal Cu–Au deposits. Philippines. Econ. Geo. 93 (4), 373–404.
Heydari, E., Moore, C.H., 1989. Burial diagenesis and thermochemical sulfate reduction, Smackover Formation, southeastern Mississippi salt basin. Geology 17 (12), 1080–1084.
Hou, Z.Q., Yang, Y.Q., Qu, X.M., Huang, D.H., Lu, Q.T., 2004. Tectonic evolution and mineralization systems of the Yidun arc orogen in sanjiang region, china. Acta Geol. Sin. 78 (1), 109–120 (in Chinese with English abstract).
Hou, Z.Q., Zaw, K., Pan, G.T., Mo, X.X., Xu, Q., Hu, Y.Z., Li, X.Z., 2007. Sanjiang Tethyan metallogenesis in SW China: tectonic setting, metallogenic epochs and deposit types. Ore Geo. Rev. 31, 48–87.
Kwak, T.A.P., Tan, T.H., 1981. The importance of $CaCl_2$ in fluid composition trends; evidence from the King Island (Dolphin) skarn deposit. Econ. Geo. 76 (4), 955–960.
Leng, C.B., Cooke, D.R., Hou, Z.Q., Evans, N.J., Zhang, X.C., Chen, W.T., Danišík, M., McInnes, B.I.A., Yang, J.H., 2018. Quantifying exhumation at the giant Pulang porphyry Cu–Au deposit using U-Pb–He dating. Econ. Geol. 113 (5), 1077–1092.
Leng, C.B., Huang, Q.Y., Zhang, X.C., Wang, S.X., Zhong, H., Hu, R.Z., Bi, X.W., Zhu, J.J., Wang, X.S., 2014. Petrogenesis of the late Triassic volcanic rocks in the southern Yidun arc, SW China: constraints from the geochronology, geochemistry, and Sr–Nd–Pb–Hf isotopes. Lithos 190–191, 363–382.
Leng, C.B., Zhang, X.C., Hu, R.Z., Wang, S.X., Zhong, H., Wang, W.Q., Bi, X.W., 2012. Zircon U-Pb and molybdenite Re–Os geochronology and Sr–Nd–Pb–Hf isotopic constraints on the genesis of the Xuejiping porphyry copper deposit in Zhongdian, Northwest Yunnan, China. J. Asian Earth Sci. 60, 31–48.
Lu, H.Z., Fan, H.R., Ni, P., Ou, G.X., Shen, K., Zhang, W.H., 2004. Fluid inclusion. Science Press, Beijing 36–228 (in Chinese).
McCrea, J.M., 1950. On the isotopic chemistry of carbonates and a paleotemperature scale. J. Chem. Phys. 18 (6), 849–857.
Meinert, L.D., 1982. Skarn, manto, and breccia pipe formation in sedimentary rocks of the Cananea mining district, Sonora. Mexico. Econ. Geo. 77 (4), 919–949.
Morley, C.K., 2012. Late Cretaceous-Early Palaeogene tectonic development of SE Asia. Earth Sci. Rev. 115 (1–2), 37–75.
Naden, J., Shepherd, T.J., 1989. Role of methane and carbon dioxide in gold deposition. Nature 342, 93–795.
O'Neil, J.R., Clayton, R.N., Mayeda, T.K., 1969. Oxygen isotope fractionation in divalent metalcarbonates. J. Chem. Phys. 51 (12), 5547–5558.
Peng, H.J., Mao, J.W., Hou, L., Shu, Q.H., Zhang, C.Q., Liu, H., Zhou, Y.M., 2016. Stable isotope and fluid inclusion constraints on the source and evolution of ore fluids in the Hongniu-Hongshan Cu skarn deposit, Yunnan Province, China. Econ. Geo. 111 (6), 1369–1396.
Potter, J., Konnerup-Madsen, J., 2003. A review of the occurrence and origin of abiogenic hydrocarbons in igneous rocks. Geol. Soc. London Spec. Publ. 214, 151–173.
Ray, J.S., Ramesh, R., Pande, K., Trivedi, J.R., Shukla, P.N., Patel, P.P., 2000. Isotope and rare earth element chemistry of carbonatite-alkaline complexes of Deccan volcanic province: implications to magmatic and alteration processes. J. Asian Earth Sci. 18 (2), 177–194.
Ren, T., Zhang, X.C., Han, R.S., Ma, M.J., 2013. Petrogenesis of the Langdu high-K calc-alkaline intrusions in Yunnan Province: constraints from geochemistry and Sr–Nd isotopes. Acta Geol. Sin. 87 (2), 454–466.
Ren, T., Zhong, H., Zhang, X.C., Zhu, W.G., 2010. REE geochemistry of garnets from the Langdu skarn copper deposit. Geosci. Front. 17 (2), 348–358.
Roedder, E., 1984. Fluid inclusions. Rev. Mineral. 12, 646 pp.
Rosenbaum, J., Sheppard, S.M.F., 1986. An isotopic study of siderites, dolomites and ankerites at high temperatures. Geochim. Cosmochim. Acta 50 (6), 1147–1150.
Rowins, S.M., 2000. Reduced porphyry copper-gold deposits: a new variation on an old theme. Geology 28 (6), 491–494.
Ruano, S.M., Both, R.A., Golding, S.D., 2002. A fluid inclusion and stable isotope study of the Moonta copper-gold deposits, South Australia: evidence for fluid immiscibility in a magmatic hydrothermal system. Chem. Geol. 192 (3–4), 211–226.
Salvi, S., Williams-Jones, A.E., 1997. Fischer-Tropsch synthesis of hydrocarbons during sub-solidus alteration of the Strange Lake peralkaline granite, Quebec/Labrador, Canada. Geochim. Cosmochim. Acta 61 (1), 83–99.
Sheppard, S.M.F., 1986. Characterization and isotopic variations in natural waters. Rev. Mineral. Geochem. 16, 165–183.
Taylor, H.P., 1979. Oxygen and hydrogen isotope relationships in hydrothermal mineral deposits. In: Barnes, H.L. (Ed.), Geochemistry of Hydrothermal Ore Deposits, 2nd ed. Wiley, New York, pp. 236–277.
Tian, Z.D., Leng, C.B., Zhang, X.C., Zafar, T., Zhang, L.J., Hong, W., Lai, C.K., 2019. Chemical composition, genesis and exploration implication of garnet from the Hongshan Cu–Mo skarn deposit, SW China. Ore Geol. Rev. 112, 103016.
Ueda, A., Sakai, H., 1984. Sulfur isotope study of Quaternary volcanic rocks from the Japanese island arc. Geochim. Cosmochim. Acta 48 (9), 1837–1848.
Van den Kerkhof, A., Thiéry, R., 2001. Carbonic inclusions. Lithos 55 (1–4), 49–68.
Wang, S.X., Zhang, X.C., Leng, C.B., Qin, C.J., 2007. A tentative study of ore geochemistry and ore-forming mechanism of Pulang porphyry copper deposit in Zhongdian, northwestern Yunnan. Miner. Deposits 26 (3), 278–288 (in Chinese with English abstract).
Wang, S.X., Zhang, X.C., Leng, C.B., Qin, C.J., Wang, W.Q., Zhao, M.C., 2008a. Stable isotopic compositions of the Hongshan skarn copper deposit in the Zhongdian area and its implication for the copper mineralization process. Acta Petrol. Sin. 24 (3), 480–488 (in Chinese with English abstract).
Wang, X.S., Bi, X.W., Leng, C.B., Zhong, H., Tang, H.F., Chen, Y.W., Yin, G.H., Huang, D.Z., Zhou, M.F., 2014. Geochronology and geochemistry of Late Cretaceous igneous intrusions and Mo–Cu–(W) mineralization in the southern Yidun Arc, SW China: implications for metallogenesis and geodynamic setting. Ore Geol. Rev. 61, 73–95.
Wang, T.G., Ni, P., Wang, G.G., Zhang, T., 2008b. Identification and significance of methane-rich fluid inclusions in Changba Pb–Zn deposit. Gansu Province. Acta Petrol. Sinica 24 (9), 2105–2112 (in Chinese with English abstract).
Wen, C.H., Shao, Y.J., Li, B., Dick, J.M., Lai, J.Q., Huang, G.F., Luo, X.Y., 2019. Fluid evolution of the Wushan skarn-dominant copper deposit in the Middle-Lower Yangtze River metallogenic belt, Eastern China. Ore Geo. Rev. 112, 103035.
Yang, Y.Q., Hou, Z.Q., Huang, D.H., Qu, X.M., 2002. Collision orogenic process and magmatic metallogenic system in Zhongdian arc. Acta Geosci. Sin. 23 (1), 17–24 (in Chinese with English abstract).
Zhang, K.J., Zhang, Y.X., Tang, X.C., Xia, B., 2012. Late Mesozoic tectonic evolution and growth of the Tibetan plateau prior to the Indo-Asian collision. Earth Sci. Rev. 114 (3–4), 236–249.
Zhang, W., Williams-Jones, A.E., Leng, C.B., Zhang, X.C., Chen, W.T., Qin, C.J., Su, W.C., Yan, J.H., 2019. The origin of CH_4-rich fluids in reduced porphyry-skarn Cu–Mo–Au systems. Ore Geol. Rev. 114, 103135.
Zeng, P.S., Wang, H.P., Mo, X.X., Yu, X.H., Li, W.C., Li, T.G., Li, H., Yang, C.Z., 2004. Tectonic setting and prospects of porphyry copper deposits in Zhongdian island arc belt. Acta Geosci. Sin. 25, 535–540 (in Chinese with English abstract).
Zheng, Y.F., 1993a. Calculation of oxygen isotope fractionation in anhydrous silicate minerals. Geochim. Cosmochim. Acta 57 (5), 1079–1091.
Zheng, Y.F., 1993b. Calculation of oxygen isotope fractionation in hydroxyl-bearing silicates. Earth Planet. Sci. Lett. 120 (3–4), 247–263.
Zheng, Y.F., 2001. Theoretical modeling of stable isotope systems and its applications to geochemistry of hydrothermal ore deposits. Miner. Deposits 20 (1), 57–70 (in Chinese with English abstract).
Zhu, D.C., Zhao, Z.D., Niu, Y.L., Mo, X.X., Chung, S.L., Hou, Z.Q., Wang, L.Q., Wu, F.Y., 2011. The Lhasa Terrane: record of a microcontinent and its histories of drift and growth. Earth Planet. Sci. Lett. 301 (1–2), 241–255.